Simulation of a tangential soft x-ray imaging system[a)]

D. J. Battaglia,[1,b)] M. W. Shafer,[1] E. A. Unterberg,[1] R. E. Bell,[2] D. L. Hillis,[1] B. P. LeBlanc,[2] R. Maingi,[1] S. Sabbagh,[3] and B. C. Stratton[2]

[1]*Oak Ridge National Laboratory, Oak Ridge, Tennessee 37831, USA*
[2]*Princeton Plasma Physics Laboratory, Princeton, New Jersey 08543, USA*
[3]*Columbia University, New York, New York 10027, USA*

Tangentially viewing soft x-ray (SXR) cameras are capable of detecting nonaxisymmetric plasma structures in magnetically confined plasmas. They are particularly useful for studying stationary perturbations or phenomenon that occur on a timescale faster than the plasma rotation period. Tangential SXR camera diagnostics are planned for the DIII-D and NSTX tokamaks to elucidate the static edge magnetic structure during the application of 3D perturbations. To support the design of the proposed diagnostics, a synthetic diagnostic model was developed using the CHIANTI database to estimate the SXR emission. The model is shown to be in good agreement with the measurements from an existing tangential SXR camera diagnostic on NSTX. © *2010 American Institute of Physics.* [doi:10.1063/1.3478883]

I. INTRODUCTION

High-temperature tokamak plasmas radiate significant power in the soft x-ray (SXR) energy range ($h\nu \sim 0.1-10$ keV). Imaging the SXR emission tangentially to the magnetic axis is an effective technique for detecting nonaxisymmetric perturbations in the plasma that either do not rotate (i.e., locked modes) or occur on a fast timescale compared to the rotation period (i.e., sawtooth crashes).[1] Fast-framing SXR camera diagnostics have been used to measure both rotating and nonrotating core magnetic islands in magnetically confined plasmas on TEXTOR,[1] LHD,[2] and NSTX.[3]

SXR camera systems that can image the SXR emission from the edge plasma region during the application of magnetic field perturbations are planned for the DIII-D and NSTX tokamaks. These externally applied 3D magnetic fields ($\delta B/B \sim 10^{-4}-10^{-3}$ at the outboard midplane) have been utilized to alter edge-localized mode (ELM) stability including complete suppression of ELMs on DIII-D (Ref. 4) and triggering of ELMs during otherwise ELM-free periods on NSTX.[5]

The magnetic perturbations are predicted to induce small (1–20 cm) edge-localized magnetic islands that alter the transport near the H-mode pedestal. The island structure may be influenced by the plasma response to the perturbations, including magnetic shielding due to plasma flows[6] and amplification due to resonances.[7] Extrapolating this ELM stability control technique to ITER and other tokamak reactor designs requires an understanding of the influence the plasma response has on the penetration of the 3D field perturbations past the plasma edge.

The proposed SXR edge imaging diagnostics on DIII-D and NSTX would provide complimentary measurements for benchmarking theoretical and computational models. The proposed diagnostics are similar to the SXR imaging diagnostics that have measured core MHD (~ 10 cm) at fast frame rates (~ 50 kHz), but will trade off speed (~ 1 kHz) for spatial resolution (~ 0.2 cm). The longer integration time relies on the assumption that the magnetic structure of interest is locked to the static externally applied perturbation.

This paper describes a synthetic diagnostic model developed as a design tool for the proposed SXR edge imaging systems. The model is benchmarked against existing data from a fast SXR core imaging camera presently on NSTX. The synthetic diagnostic is in good agreement with the experimental data, which provides confidence that it is a suitable tool for testing the design of the proposed edge imaging systems.

II. SYNTHETIC DIAGNOSTIC MODEL

The x-ray emission spectrum, $j(\nu)$, is computed using CHIANTI, an atomic database for spectroscopic diagnostics of astrophysical plasmas.[8,9] CHIANTI provides analytic tools to compute the free-free (Bremsstrahlung) and free-bound (recombination) electron radiation, as well as the bound electron radiation (spectral line emission) in a plasma. The calculations presented in this paper employ the Mazzotta *et al.*[10] ionization model. A large look-up table of emission spectrums is compiled for a variety of atomic numbers (Z) and electron temperatures (T_e). The ratios of the spectral lines have a weak dependence on n_e and a plasma density of 10^{13} cm^{-3} is assumed for the calculation.

An SXR emission model described by von Goeler *et al.*[1] is appropriate for estimating the signal for SXR imaging diagnostics on tokamaks when a spectral filter is used to cutoff the low energy spectrum (typically below 1 keV) and the

plasma is composed of only hydrogen and carbon. However, the recent interest in imaging the lower temperature SXR edge emission necessitates a lower filter cutoff (0.5–1.0 keV) and therefore a more complete model, like CHIANTI, that includes the large contributions from impurity ion spectra below 1 keV. Furthermore, the CHIANTI database provides an opportunity to examine the contributions from other trace impurity ions found in tokamak plasmas (i.e., oxygen, nitrogen, iron).

The SXR imaging diagnostics under consideration use a pinhole to image the SXR emission onto a scintillator that converts the x-ray photons to visible photons. The trajectory of the optical axis through the plasma is computed for each scintillator pixel. The total power of the visible photons emitted by a scintillator pixel due to x-rays originating from a unit volume of plasma at a point on the optical axis (L) is

$$g[\text{keV s}^{-1}\text{ cm}^{-3}] = 4\pi n_e \sum_Z n_Z \int_0^\infty j(Z, T_e, h\nu)\varepsilon(h\nu)dh\nu, \tag{1}$$

where n_e is the local electron density, n_z is the local density of each ion species, and T_e is the local electron temperature. The conversion efficiency, $\varepsilon(h\nu)$, incorporates the quantum efficiency of the scintillator and the spectral transmission of the diagnostic filter.[11]

The pixel brightness, f_{pix}, is the total radiated power per unit volume integrated over the optical axis,

$$f_{\text{pix}}[\text{keV s}^{-1}\text{ cm}^{-2}] = \int g(L)dL. \tag{2}$$

Thus, the power radiated from each scintillator pixel (assuming the pinhole aperture is parallel to the plane of the scintillator) is approximately[12]

$$P[\text{keV s}^{-1}] = (A_{ap}A_{\text{pix}}d_s^2/4\pi d_l^4)f_{\text{pix}}, \tag{3}$$

where A_{ap} is the area of the pinhole, A_{pix} is the area of the pixel, d_s is the separation of the center of the scintillator and the pinhole, and d_l is the distance between the pinhole and the pixel. This calculation is performed for each scintillator pixel in order to create a 2D image. Finally, the image is multiplied by the camera integration time and the total conversion efficiency of the imaging system (digitizer counts per visible photon energy) to get the total expected digitizer counts for each camera pixel.

III. COMPARISON TO EXPERIMENTAL DATA

The model outlined in Sec. II is compared against data from the fast SXR imaging camera (FSXIC) on NSTX.[3,13] The field of view of the camera includes the entire radial extent of the plasma and nearly the entire height. The diagnostic uses a pinhole to image SXR emission onto a P47 scintillator screen that converts x-rays to visible light. The system has interchangeable pinholes and filter materials that are remotely selected using motor driven pistons. The visible image is intensified and demagnified by an electrostatic image intensifier and imaged onto a fast framing CCD camera manufactured by Princeton Scientific Instruments, Inc.
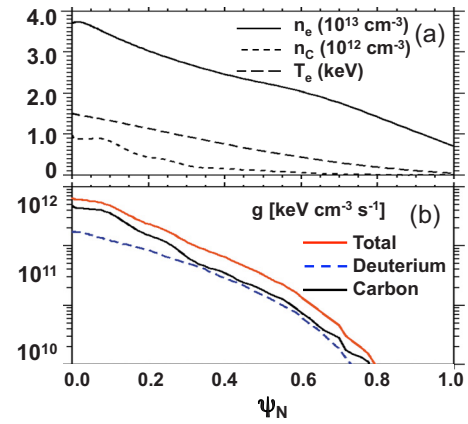

FIG. 1. (Color online) (a) Plasma profiles near $t=310$ ms for discharge 115840. (b) X-ray emission vs ψ_N. The red/gray line is the sum of the carbon (black) and deuterium (dashed blue/gray) contributions.

(Princeton, NJ) The camera can capture up to 300 frames and operate with frame rates up to 500 kHz at 64×64 resolution.

The model of the FSXIC camera has been compared against data from a variety of discharges on NSTX. The best agreement is typically observed in L-mode discharges that have a relatively modest plasma density ($<5\times10^{13}$ cm^{-3}) and carbon density ($<0.1\times10^{13}$ cm^{-3}).

The electron temperature, electron density, and carbon density (n_C) profiles for a representative L-mode discharge are shown in Fig. 1(a) (discharge 115840). The profiles are mapped to the normalized poloidal flux (ψ_N) using a calculation of the plasma equilibrium. The total radiated power per unit volume is calculated using these profiles and is shown versus ψ_N in Fig. 1(b). The x-ray emission from the colder edge is excluded using a 7.6 um beryllium filter. Most of the radiated power in the plasma core is attributed to continuum radiation from carbon ions.

The details of the FSXIC diagnostic are taken directly from the values published by Stratton *et al.*[13] For discharge 115840, the pinhole size is 3 mm and the integration time is 50 μs. The average of four frames measured by the FSXIC is shown in Fig. 2(a). The horizontal line across the image is an artifact of the CCD chip. The two vertical lines are due to thin wires that were temporary added to aid in focusing and aiming the camera. The center column of the tokamak is just outside the field of view to the left of the image, while the outboard limiter is at the right edge of the image.

In contrast to the good agreement observed with L-mode discharges, the synthetic diagnostic calculations for recent
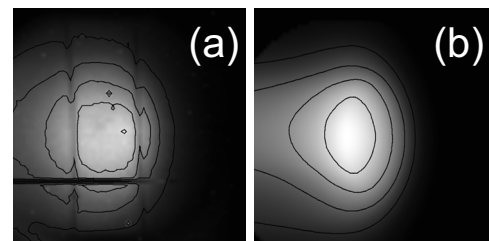

FIG. 2. (a) Average of the first four frames of the raw FSXIC data for 115840 at $t=310$ ms. (b) Synthetic diagnostic image displayed using the same scale.
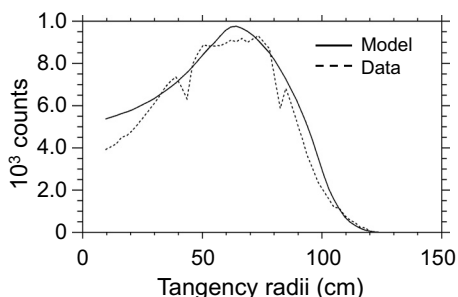
FIG. 3. Signal on the center row of pixels in the raw data and the simulated image vs tangency radii.

ELM-free H-mode discharges on NSTX have been consistently lower than the raw FSXIC data. In Fig. 3, the signal across the center of the images (row 30) is compared. Good agreement is achieved between the model and the raw data from the FSXIC for this standard L-mode discharge. The largest differences are near the left edge of the image, which may be a result of vignetting in the visual optics.

IV. DISCUSSION AND SUMMARY

The agreement between the synthetic diagnostic and the FSXIC data suggests that the SXR radiation in modest-density, deuterium L-mode discharges on NSTX can be adequately described using the spectra attributed to deuterium and carbon. This is reasonable, since carbon is routinely measured to be the dominant impurity species due to the fact that the first wall of NSTX is a composite of carbon.

The synthetic diagnostic calculations for recent ELM-free H-mode discharges on NSTX have been consistently lower than the raw FSXIC data. This discrepancy, sometimes as large as a factor of four, can be attributed to the build-up of impurities other than carbon in the presence of an edge transport barrier. For example, the discrepancy is resolved for these discharges when an iron density of the order of 0.5% of the carbon density is added to the simulation.

Typically, the assumptions used in CHIANTI such as a Maxwellian electron velocity distribution and complete ionization equilibrium become less valid in tokamak plasmas due to significant time-evolving neutral beam injection, radio-frequency heating, and neutral fueling. Thus, the agreement between the synthetic diagnostic and the SXR imaging data on NSTX also indicates that the assumptions do not introduce significant error when modeling the radiation from the core of high-temperature tokamak plasma. Consequently, the model presented in this paper is useful for quick estimates of signal strength and is well suited for optimization of potential diagnostic designs.

This synthetic diagnostic model is currently used by Shafer[14] to evaluate a proposed design for a SXR edge imaging diagnostic for DIII-D. In these calculations, the position and size of the induced magnetic islands are modeled using TRIP3D.[15] The effect of the islands on the local x-ray emissivity is approximated by assuming the parameters along each field line are fixed by the values at the starting point of the field line (i.e., negligible transport perpendicular to the magnetic field lines). Thus, the x-ray emissivity is assumed to be constant along the field lines. A variety of diagnostic designs are tried within this model in order to maximize the potential for accurately resolving the edge islands. Initial calculations suggest the proposed design will resolve the islands with sufficient contrast and spatial resolution to detect high-m (order of 10) island structures that are only several centimeters wide.

ACKNOWLEDGMENTS

[1] S. von Goeler, R. Kaita, M. Bitter, G. Fuchs, M. Poier, G. Bertschinger, H. R. Koslowski, K. Toi, S. Ohdachi, and A. Donne, Rev. Sci. Instrum. **70**, 599 (1999).

[2] S. Ohdachi, K. Toi, G. Fuchs, and S. von Goeler, Rev. Sci. Instrum. **72**, 724 (2001).

[3] C. E. Bush, B. C. Stratton, J. Robinson, L. E. Zakharov, E. D. Fredrickson, D. Stutman, and K. Tritz, Rev. Sci. Instrum. **79**, 10E928 (2008).

[4] T. E. Evans, M. E. Fenstermacher, R. A. Moyer, T. H. Osborne, J. G. Watkins, P. Gohil, I. Joseph, M. J. Schaffer, L. R. Baylor, M. Bécoulet, J. A. Boedo, K. H. Burrell, J. S. deGrassie, K. H. Finken, T. Jernigan, M. W. Jakubowski, C. J. Lasnier, M. Lehnen, A. W. Leonard, J. Lonnroth, E. Nardon, V. Parail, O. Schmitz, B. Unterberg, and W. P. West, Nucl. Fusion **48**, 024002 (2008).

[5] J. M. Canik, R. Maingi, T. E. Evans, R. E. Bell, S. P. Gerhardt, B. P. LeBlanc, J. Manickam, J. E. Menard, T. H. Osborne, J.-K. Park, S. F. Paul, P. B. Snyder, S. A. Sabbagh, H. W. Kugel, and E. A. Unterberg, Phys. Rev. Lett. **104**, 045001 (2010).

[6] M. Bécoulet, G. Huysmans, X. Garbet, E. Nardon, D. Howell, A. Garofalo, M. Schaffer, T. Evans, K. Shaing, A. Cole, J.-K. Park, and P. Cahyna, Nucl. Fusion **49**, 085011 (2009).

[7] A. Boozer, Phys. Rev. Lett. **86**, 5059 (2001).

[8] K. P. Dere, E. Landi, H. E. Mason, B. C. Monsignori Fossi, and P. R. Young, A&AS **125**, 149 (1997).

[9] K. P. Dere, E. Landi, P. R. Young, G. Del Zanna, M. Landini, and H. E. Mason, A&A **498**, 915 (2009).

[10] P. Mazzotta, G. Mazzitelli, S. Colafrancesco, and N. Vittorio, A&AS **133**, 403 (1998).

[11] B. L. Henke, E. M. Gullikson, and J. C. Davis, At. Data Nucl. Data Tables **54**, 181 (1993).

[12] R. S. Granetz and P. Smeulders, Nucl. Fusion **28**, 457 (1988).

[13] B. C. Stratton, R. Feder, S. von Goeler, G. F. Renda, V. J. Mastrocola, and J. L. Lowrance, Rev. Sci. Instrum. **75**, 3959 (2004).

[14] M. W. Shafer, D. J. Battaglia, E. A. Unterberg, T. E. Evans, D. L. Hillis, and R. Maingi, Rev. Sci. Instrum. **81**, 10E534 (2010).

[15] T. E. Evans, R. A. Moyer, and P. Monat, Phys. Plasmas **9**, 4957 (2002).